

## Article

# Shape Anisotropy of Grains Formed by Laser Melting of (CoCuFeZr)<sub>17</sub>Sm<sub>2</sub>

Felix Trauter \*, Ralf Loeffler, Gerhard Schneider and Dagmar Goll \*

Materials Research Institute, Aalen University, 73430 Aalen, Germany; ralf.loeffler@hs-aalen.de (R.L.); gerhard.schneider@hs-aalen.de (G.S.)

\* Correspondence: felix.trauter@hs-aalen.de (F.T.); dagmar.goll@hs-aalen.de (D.G.);  
Tel.: +49-7361-576-1672 (F.T.); +49-7361-576-1601 (D.G.)

**Abstract:** For permanent magnetic materials, anisotropic microstructures are crucial for maximizing remanence  $J_r$  and maximum energy product  $(BH)_{\max}$ . This also applies to additive manufacturing processes such as laser powder bed fusion (PBF-LB). In PBF-LB processing, the solidification behavior is determined by the crystal structure of the material, the substrate, and the melt-pool morphology, resulting from the laser power  $P_L$  and scanning speed  $v_s$ . To study the impact of these parameters on the textured growth of grains in the melt-pool, experiments were conducted using single laser tracks on (CoCuFeZr)<sub>17</sub>Sm<sub>2</sub> sintered magnets. A method was developed to quantify this grain shape anisotropy from electron backscatter diffraction (EBSD) analysis. For all grains in the melt-pool, the grain shape aspect ratio (GSAR) is calculated to distinguish columnar (GSAR < 0.5) and equiaxed (GSAR > 0.5) grains. For columnar grains, the grain shape orientation (GSO) is determined. The GSO represents the preferred growth direction of each grain. This method can also be used to reconstruct the temperature gradients present during solidification in the melt-pool. A dependence of the melt-pool aspect ratio (depth/width) on energy input was observed, where increasing energy input (increasing  $P_L$ , decreasing  $v_s$ ) led to higher aspect ratios. For aspect ratios around 0.3, an optimum for directional columnar growth (93% area fraction) with predominantly vertical growth direction (mean angular deviation of 23.1° from vertical) was observed. The resulting crystallographic orientation is beyond the scope of this publication and will be investigated in future work.

**Keywords:** additive manufacturing; laser powder bed fusion (PBF-LB); permanent magnets; tailored microstructure; Sm-Co; Sm<sub>2</sub>(CoCuFeZr)<sub>17</sub>; textured solidification; EBSD



**Citation:** Trauter, F.; Loeffler, R.; Schneider, G.; Goll, D. Shape Anisotropy of Grains Formed by Laser Melting of (CoCuFeZr)<sub>17</sub>Sm<sub>2</sub>. *Metals* **2024**, *14*, 1025. <https://doi.org/10.3390/met14091025>

Academic Editors: Dan Wang and Zeyu Wang

Received: 8 August 2024

Revised: 5 September 2024

Accepted: 6 September 2024

Published: 9 September 2024



**Copyright:** © 2024 by the authors. Licensee MDPI, Basel, Switzerland. This article is an open access article distributed under the terms and conditions of the Creative Commons Attribution (CC BY) license (<https://creativecommons.org/licenses/by/4.0/>).

## 1. Introduction

Additive manufacturing technologies such as laser powder bed fusion (PBF-LB) open up new possibilities for the production of components with complex geometries and optimized topologies that are difficult or impossible to achieve using conventional processes. Additionally, PBF-LB enables functional integration and individually tailored microstructures and properties. For the processing of permanent magnets, a textured microstructure is of special interest to achieve the best possible magnetic properties (remanence  $J_r$  and maximum energy product  $(BH)_{\max}$ ) [1,2]. Permanent magnets with high texture grades (~98%) are conventionally manufactured by powder metallurgical processes. Achieving a high degree of texture in PBF-LB, however, remains a major challenge. Until now, only partially anisotropic microstructures were achieved by PBF-LB processing for permanent magnets based on FeNdB [3], (CoCuFeZr)<sub>17</sub>Sm<sub>2</sub> [4], and FePrCuB [5]. While anisotropic microstructures in PBF-LB manufactured rare earth (RE)-based permanent magnets were first published in FeNdB by Goll et al. [3] the samples did not exhibit high coercivities. The reason for the low coercivities was found to be the size of the hard magnetic grains, which solidified in dendrites with a length of >50 μm [6]. So far, all FeNdB magnets produced by PBF-LB that showed high coercivities were found to be largely isotropic. This was the case

in samples produced from the commercially available Fe-rich FeNdB-alloy Magnequench MQP-S [7–10] as well as in samples with customized alloy compositions [11,12].

So far, FePrCuB and  $\text{Co}_{17}\text{Sm}_2$  are the only RE-based permanent magnet materials that have achieved both significant texture and high coercivity by PBF-LB processing. It is well known that anisotropic microstructures occur in FePrCuB alloys (e.g., by directional solidification at the mold wall during casting) [13–15]. The anisotropic microstructure is preserved during the annealing process, leading to magnetic anisotropy and thus increased remanence. Recently, FePrCuB alloys were also processed using PBF-LB [5,16]. Schäfer et al. [16] compared the properties of Fe73.5-Pr21.0-Cu2.0-B3.5 suction cast samples with a few layers of material built up in the PBF-LB process. The first PBF-LB processed FePrCuB magnet with partial anisotropy was produced by Goll et al. [5], using the composition Fe73.8-Pr20.5-Cu2.0-B3.7. Using EBSD analysis of the microstructure in the as-built condition as well as after annealing, it was shown that the grains have a preferred growth direction along the building direction, which leads to preferred alignment of the easy axis of the magnetization (*c*-axis, <001> crystal direction) along the scanning direction. Measured with the magnetic field along the scanning direction, the sample achieved a coercivity of  $\mu_0 H_c = 0.67$  T, a remanence of  $J_r = 0.67$  T, and a maximum energy product of  $(BH)_{\max} = 69.8$  kJ/m<sup>3</sup>. The remanence along the scanning direction (0.67 T) is about three times higher than along the building direction (0.26 T).  $(\text{CoCuFeZr})_{17}\text{Sm}_2$  has also proven to be a promising material for PBF-LB processing, where columnar dendritic growth of the grains along the building direction was observed [2]. The crystallographic anisotropy was preserved during the three-step annealing procedure necessary to obtain favorable magnetic properties. After annealing, the crystallographic anisotropy also leads to anisotropy of the magnetic properties, with an increased remanence parallel to the scanning direction. With a coercivity of  $\mu_0 H_c = 2.77$  T, a remanence of  $J_r = 0.78$  T, and a maximum energy product of  $(BH)_{\max} = 109.4$  kJ/m<sup>3</sup>, it exceeded the remanence and maximum energy product of an isotropic sintered magnet of similar composition ( $J_r = 0.63$  T;  $(BH)_{\max} = 71.5$  kJ/m<sup>3</sup>) by 24% and 53%, respectively [4]. Anisotropic sintered magnets of comparable compositions of  $(\text{CoCuFeZr})_{17}\text{Sm}_2$  achieve remanences up to  $J_r = 1.1$  T and maximum energy products up to  $(BH)_{\max} = 225$  kJ/m<sup>3</sup> (e.g., Recoma 28HE [17]). These properties show the potential for PBF-LB manufactured magnets if the texture grade of anisotropic sintered magnets could be realized. This leads to the question of how the anisotropy in such PBF-LB manufactured magnets can be controlled and maximized.

Additive manufacturing of functional materials is still a comparatively new field of research, and publications of in-depth research on specific topics are rather rare. However, some of these topics are well-studied on more common structural materials such as steels, aluminum alloys, titanium alloys, or nickel alloys. The knowledge from these materials can provide guidelines to achieve better textures in additively manufactured functional materials as well, although results have to be validated and adapted for their more complex phase compositions, crystallographic structures, and solidification behavior.

In general, the microstructure of PBF-LB manufactured samples is always the result of melting and solidification of material in the melt-pool produced by the laser [18,19]. Following that, the fundamental prerequisite for a textured microstructure is directional solidification inside the melt-pool. In principle, the solidification microstructure is dominated by the temperature gradient *G* and the growth rate *R*, as well as the crystallographic structure. While the ratio of *G/R* determines the growth form and type, the product of *G*·*R* determines the resulting grain size (Figure 1). To achieve a microstructure with anisotropic properties, columnar dendritic growth has to occur. During columnar dendritic growth, dendritic grains grow with the preferred growth direction of the crystal structure along the temperature gradient [20]. According to Kurz and Fisher [20], the preferred growth direction of the binary  $\text{Co}_{17}\text{Sm}_2$  phase is the <0001> crystal direction. A pronounced <0001> texture along the growth direction was also found in  $(\text{CoCuFeZr})_{17}\text{Sm}_2$  single crystals prepared by zone melting with low growth rates [21]. Contrary to that, in previous research on PBF-LB processing of  $(\text{CoCuFeZr})_{17}\text{Sm}_2$ , the <0001> crystal direction was found to be

mostly perpendicular to the preferred growth direction of the grains [4]. This difference in the preferred growth direction was also reported by Plugaru et al. [22], who found a transition of preferred growth along the  $\langle 0001 \rangle$  direction to perpendicular to it when increasing the floating zone velocity during unidirectional solidification of  $(\text{CoCuFeZr})_{17}\text{Sm}_2$  alloys. During laser melting processes such as PBF-LB processing, the conditions are especially favorable for columnar dendritic growth. This is due to the fact that the laser melting causes localized overheating of the melt. This leads to extremely high temperature gradients and high solidification velocities [23]. As a positive side effect, this often causes a suppression of the growth of secondary dendrite arms (constrained dendritic growth) [24]. Such secondary dendrite arms could disrupt the primary solidification texture.

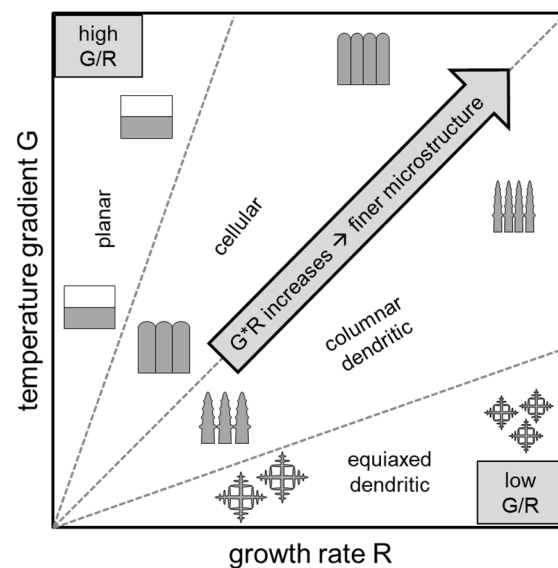


**Figure 1.** Influence of temperature gradient  $G$  and growth rate  $R$  on the morphology ( $G/R$ ) and fineness ( $G \cdot R$ ) of the solidification microstructure (Adapted from [25]).

In the laser melt-pool, the temperature gradient is approximately perpendicular to the melt-pool interface (see black arrows in Figure 2), while the  $G$  and  $R$  values vary strongly along the solid–liquid interface [26]. The highest values for  $G$  are found at the bottom of the melt-pool and decrease along the sides towards the surface of the melt-pool and along the scan vector towards the already solidified part of the scan-track. In contrast, the highest values for the parameter  $R$  are found at the melt-pool surface and decrease towards the solid–liquid interface [27,28]. This means that the solidification conditions and resulting microstructures are highly dependent upon the melt-pool characteristics (depth, width), which in turn are determined by the laser processing parameters as illustrated in Figure 2. Considering a single laser track or single melt-pool, only the laser intensity  $I_L$  (or simplified by assuming a constant laser spot size, the laser power  $P_L$ ), the scanning speed  $v_s$ , and the resulting line energy  $E_L$  ( $E_L = P_L/v_s$ ) determine the melt-pool characteristics [29]. Generally, two process regimes can take place in laser melting. Depending on the energy input, either heat conduction welding or keyhole welding takes place [30,31]. At lower energies, heat conduction welding forms shallow melt-pools without boiling and vaporizing larger quantities of material. When the energy input is increased high enough to vaporize a larger volume of material, the absorption of the laser is increased dramatically (e.g., in stainless steel from 15% in the melt in heat conduction to 65% in the metal vapor in keyhole welding [32]) and a deep channel of evaporated material (the keyhole) forms. The process regime of keyhole welding is characterized by very deep melt-pools but also causes extensive evaporation. This evaporation can affect some alloying elements more than others, which can cause a change in the composition [33]. This phenomenon can be especially detrimental for functional materials such as the permanent magnetic  $(\text{CoCuFeZr})_{17}\text{Sm}_2$  alloy presented here.

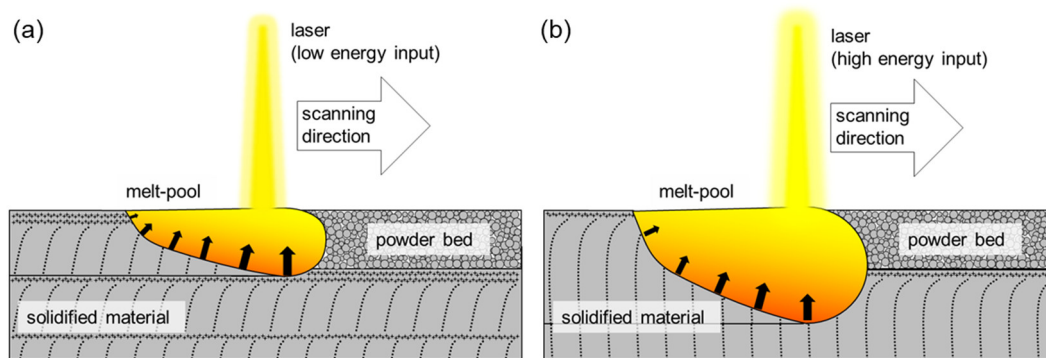


**Figure 2.** Schematic representation of the laser melt-pool formed by (a) lower and (b) higher energy input in PBF-LB additive manufacturing. For single-track experiments, the melt-pool formation is comparable to the PBF-LB process. Black arrows inside the melt-pool outline the local temperature gradient perpendicular to the melt-pool interface. The resulting microstructure with columnar grains is also shown (Adapted from [28]).

To efficiently study these laser-material interactions similarly to the PBF-LB process without the need for large amounts of powder, single-track experiments are known to be a useful tool [12,34–39]. Tosoni et al. [12] used single-track experiments to study the influence of laser power and scanning speed as well as the material’s composition on the resulting shape and geometry of the melt-pool and its microstructure in FeNdB.

In this paper, the influence of the most important laser processing parameters laser power  $P_L$  and scanning speed  $v_s$  on the textured solidification of  $(\text{CoCuFeZr})_{17}\text{Sm}_2$  in the melt-pool is analyzed. This is achieved through single-track experiments on  $(\text{CoCuFeZr})_{17}\text{Sm}_2$ -sintered magnets. To evaluate the solidification microstructure qualitatively and quantitatively, a method is developed to analyze the growth type (equiaxed–columnar) and the growth direction of grains in the melt-pool from EBSD analysis. The influence of the scanning speed, the laser power, and their mutual interaction at constant line energy is investigated in three series of experiments.

## 2. Materials and Methods

### 2.1. Sample Preparation and Measuring Equipment

To examine the influence of laser processing parameters on the solidification microstructure efficiently, single-track experiments were performed. For that, a series of single laser tracks with varying laser parameters (scanning speed  $v_s$  and laser power  $P_L$ ) were exposed on  $(\text{CoCuFeZr})_{17}\text{Sm}_2$  isotropic sintered magnets of the composition Co61.4-Cu6.2-Fe18.8-Zr1.9-Sm11.7. The  $(\text{CoCuFeZr})_{17}\text{Sm}_2$  magnets were provided by Arnold Magnetic Technologies. From previous experiments, it is known that this alloy can produce partially textured samples during laser additive manufacturing [4]. The magnets measure 25 mm × 20 mm × 3 mm ( $l \times w \times h$ ) and were each exposed with 18 single tracks, two for each parameter. To ensure even absorption of the laser on the magnets’ surfaces, the magnets were ground by hand using 220-grit SiC-paper in a linear manner perpendicular to the laser scan vector. The exposed laser tracks have a length of 12 mm, and a spacing of 1 mm between lines, and were exposed in an alternating sequence (1, 9, 2, 10, ...) to avoid local heat accumulation from track to track, which could influence the results. The experiments were performed in a laser processing chamber under Ar-atmosphere. A fiber laser (TruFiber 1000, TRUMPF, Ditzingen, Germany) with a wavelength of 1070 nm and a maximum output power of 1000 W was used to expose the samples. The laser has a focal diameter of 46  $\mu\text{m}$ , which can be defocused to produce larger laser spot diameters. Preliminary experiments were performed using laser power ranging from 50 W <  $P_L$  < 250 W; scanning speed 100 mm/s <  $v_s$  < 1000 mm/s; and laser spot sizes 46  $\mu\text{m}$  (in focus), 90  $\mu\text{m}$ , 200  $\mu\text{m}$ , and 450  $\mu\text{m}$ ; produced by defocusing the laser by 2 mm, 5 mm, and 10 mm, respectively.

For the experiments presented, a 4 by 4 matrix of parameters with  $P_L = 50$  W, 100 W, 150 W, 200 W and  $v_s = 200$  mm/s, 400 mm/s, 600 mm/s, 800 mm/s was produced, using a laser spot size of 200  $\mu\text{m}$  (5 mm defocus). After exposure, the magnets were covered and infiltrated with epoxy resin to avoid damage to the samples during the following materialographic preparation. The samples were cut using a high-precision diamond bandsaw, embedded in epoxy resin, and—after curing—mechanically ground and polished. The polished microsections were analyzed using EBSD with EDAX camera and software (Hikari, OIM v8.6 orientation imaging microscopy, EDAX-Ametek, Weiterstadt, Germany) in a scanning electron microscope (Sigma 300 VP, ZEISS, Jena, Germany). For every parameter, six microsections were produced and analyzed using light microscopy as well as scanning electron microscopy to ensure reproducibility of melt-pool depth, width, and general microstructure.

For the evaluation of the solidification microstructure in the melt-pool, a multistep processing of the EBSD data is performed in the EDAX OIM v8.6 software. This process is described in more detail in the following section.

## 2.2. Evaluation of the Solidification Texture Using EBSD Analysis

The steps that are performed to evaluate the solidification texture in the laser melt-pools are shown in Figure 3. In Step 1, the melt-pool region on which the evaluation is based on is separated from the full scan (Figure 3a,b). Figure 3a shows the IPF map of the EBSD scan, which the evaluation is based on, Figure 3b shows the IPF map of the isolated melt-pool. This step is performed manually based on the IPF-map, the image quality map and the SEM image (the latter two images are not shown). Step 2 aims to separate grains that have a clear preferred growth direction from equiaxed grains without a preferred growth direction. This is done by evaluating the grain shape aspect ratio (GSAR), which is calculated by the ratio of the shortest axis in the grain to the longest. The GSAR map is shown in Figure 3c and the corresponding quantitatively analyzed GSAR histogram in Figure 3d. Grains with  $\text{GSAR} > 0.5$  are excluded from the following steps. For Step 3, an ellipsoid fitting is performed (Figure 3e). Each grain is fitted with an ellipse, which is then used to determine the angle of the longest axis of the grain (which is parallel to the longest axis of the ellipse). The angle is given with respect to the horizontal axis in the image plane. This grain shape orientation (GSO) will be used to illustrate and quantify the textured growth in the melt-pool. To do so, the ellipse angles are divided into 4 segments in Step 4. The angle segments are as follows:

1. Segment 1: horizontally grown grains with ellipse angles from  $0^\circ$  to  $25.7^\circ$  and  $154.3^\circ$  to  $180^\circ$ .
2. Segment 2: diagonally grown grains with ellipse angles from  $25.7^\circ$  to  $51.4^\circ$  and  $128.6^\circ$  to  $154.3^\circ$ .
3. Segment 3: grains that grew almost vertically with ellipse angles from  $51.4^\circ$  to  $77.0^\circ$  and  $102.9^\circ$  to  $128.6^\circ$ .
4. Segment 4: vertically grown grains with ellipse angles from  $77.0$  to  $102.9^\circ$ .

The segment definitions, color coding, and a respective mapping using 4 colors are shown in Figure 3h,f. In the last step, the ellipse orientation angle of each grain is normalized by its grain area, and the summarized area for each angle segment is plotted in a polar plot (Figure 3g), showing the area fraction of each segment in the corresponding angular orientation.

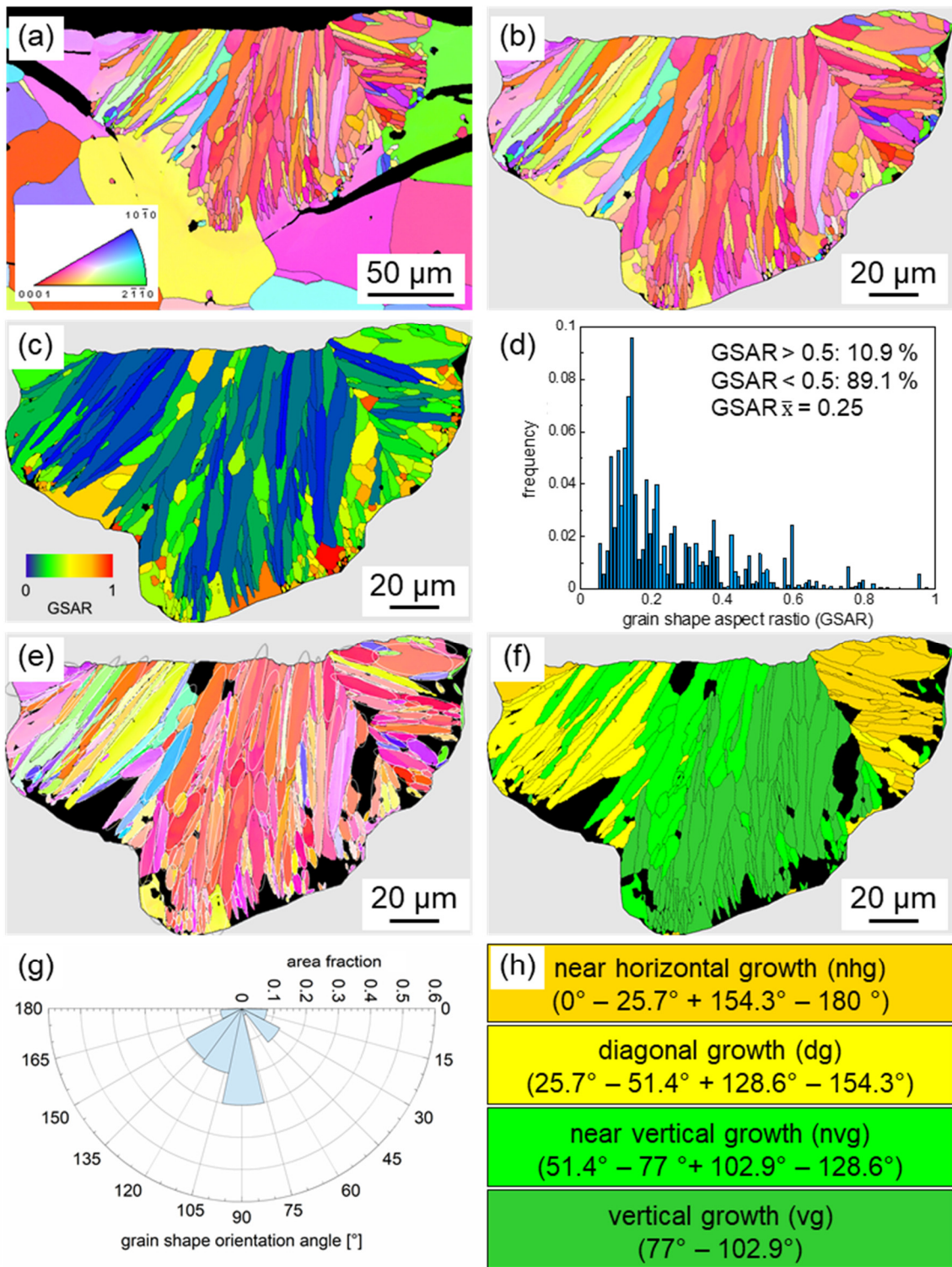


**Figure 3.** Procedure for the evaluation of the grain shape anisotropy in the melt-pool from (a) the EBSD scan (IPF map) (b) using manual separation of the melt-pool area, (c,d) grain shape aspect ratio (GSAR) evaluation to separate grains without preferential growth direction, (e) using an ellipsoid fit to determine the longest grain axis and corresponding angle, (f) visualization of the grain shape orientation (GSO) in four angular segments, (g) evaluation of the GSO in a polar diagram. The legend (h) describes the four segments of near-horizontal growth (nhg), diagonal growth (dg), near-vertical growth (nvg), and vertical growth (vg) for the GSO map.

### 3. Results

The results from the single-track experiments are presented in three sections. Each section will show the influence of one of the processing parameters  $P_L$ ,  $v_s$ , and  $E_L$ . Section 3.1 shows the influence of the laser scanning speed at a fixed laser power of 200 W. Section 3.2 shows the influence of the laser power at a fixed scanning speed of 600 mm/s. Section 3.3 shows how the melt-pool and microstructure changes at a fixed line energy of 0.25 J/mm, produced by different combinations of laser power and scanning speed.

#### 3.1. Influence of Laser Scanning Speed

The influence of the scanning speed on the melt-pool morphology and solidification behavior was examined by varying  $v_s$  (200 mm/s, 400 mm/s, 600 mm/s, 800 mm/s) and leaving  $P_L$  constant at 200 W.

The EBSD analysis of the four samples with their inverse pole figure (IPF), grain shape aspect ratio (GSAR) map, and grain shape orientation (GSO) map are given in Figure 4. In some melt-pools (e.g., Figure 4j–l), neighboring grains with low misorientation to the substrate are not recognized as individual grains in the full-area IPF map. After the isolation of the melt-pool area, the grains can be separated in the GSAR and GSO map. The parameters for the melt-pool morphology (depth, width, and aspect ratio), along with the mean GSAR values and the grain size with the d90 (90th percentile of grain size distribution) values for  $Feret_{max}$  and  $Feret_{min}$ , are listed in Table 1. The grain sizes decrease with decreasing energy input when increasing the scanning speed from 200 mm/s ( $Feret_{max}$  d90 = 96.8  $\mu\text{m}$ ,  $Feret_{min}$  d90 = 42.5  $\mu\text{m}$ ) to 600 mm/s ( $Feret_{max}$  d90 = 65.8  $\mu\text{m}$ ,  $Feret_{min}$  d90 = 11.6  $\mu\text{m}$ ) with a slight increase again at 800 mm/s ( $Feret_{max}$  d90 = 73.6  $\mu\text{m}$ ,  $Feret_{min}$  d90 = 18.6  $\mu\text{m}$ ). The mean GSAR value decreases from 0.44 at a scan speed of 200 mm/s to 0.25 at  $v_s = 600$  mm/s with a slight increase at  $v_s = 800$  mm/s to 0.30. This indicates an increase in grain area that grows columnar rather than equiaxed.

**Table 1.** Overview of the laser parameters  $P_L$ ,  $v_s$  and  $E_L$ , melt-pool size (depth and width) and aspect ratio, the grain shape aspect ratio GSAR as well as the grain size parameters  $Feret_{max}$  d90 and  $Feret_{min}$  d90 for the samples of the first series—influence of the scan speed.

Sample ( $P_L$ , $v_s$ )	Line Energy $E_L$ (J/mm)	Melt-Pool Depth ( $\mu\text{m}$ )	Melt-Pool Width ( $\mu\text{m}$ )	Melt-Pool Aspect Ratio	GSAR Mean	$Feret_{max}$ d90 ( $\mu\text{m}$ )	$Feret_{min}$ d90 ( $\mu\text{m}$ )
200 W, 200 mm/s	1.00	790	263	3.00	0.44	96.8	42.5
200 W, 400 mm/s	0.50	284	212	1.34	0.37	73.0	18.2
200 W, 600 mm/s	0.33	118	217	0.57	0.25	65.8	11.6
200 W, 800 mm/s	0.25	65	200	0.33	0.30	73.6	18.6

For the sample produced with 200 W, 200 mm/s (Figure 4a–c), a clear keyhole welding behavior is visible. It is characterized by a melt-pool that is much deeper than wide. With a depth of  $\sim 790$   $\mu\text{m}$  and a width of  $\sim 260$   $\mu\text{m}$ , the melt-pool aspect ratio is around 3. The GSAR map shows a high proportion of grains with a GSAR > 0.5, meaning equiaxed growth, especially in the lower part of the melt-pool. This area also mainly shows grains with horizontal growth direction, visible in the GSO map. In the uppermost part of the melt-pool, the grains grow more columnar with diagonal growth direction on the sides of the melt-pool and a few vertically grown grains in the center.

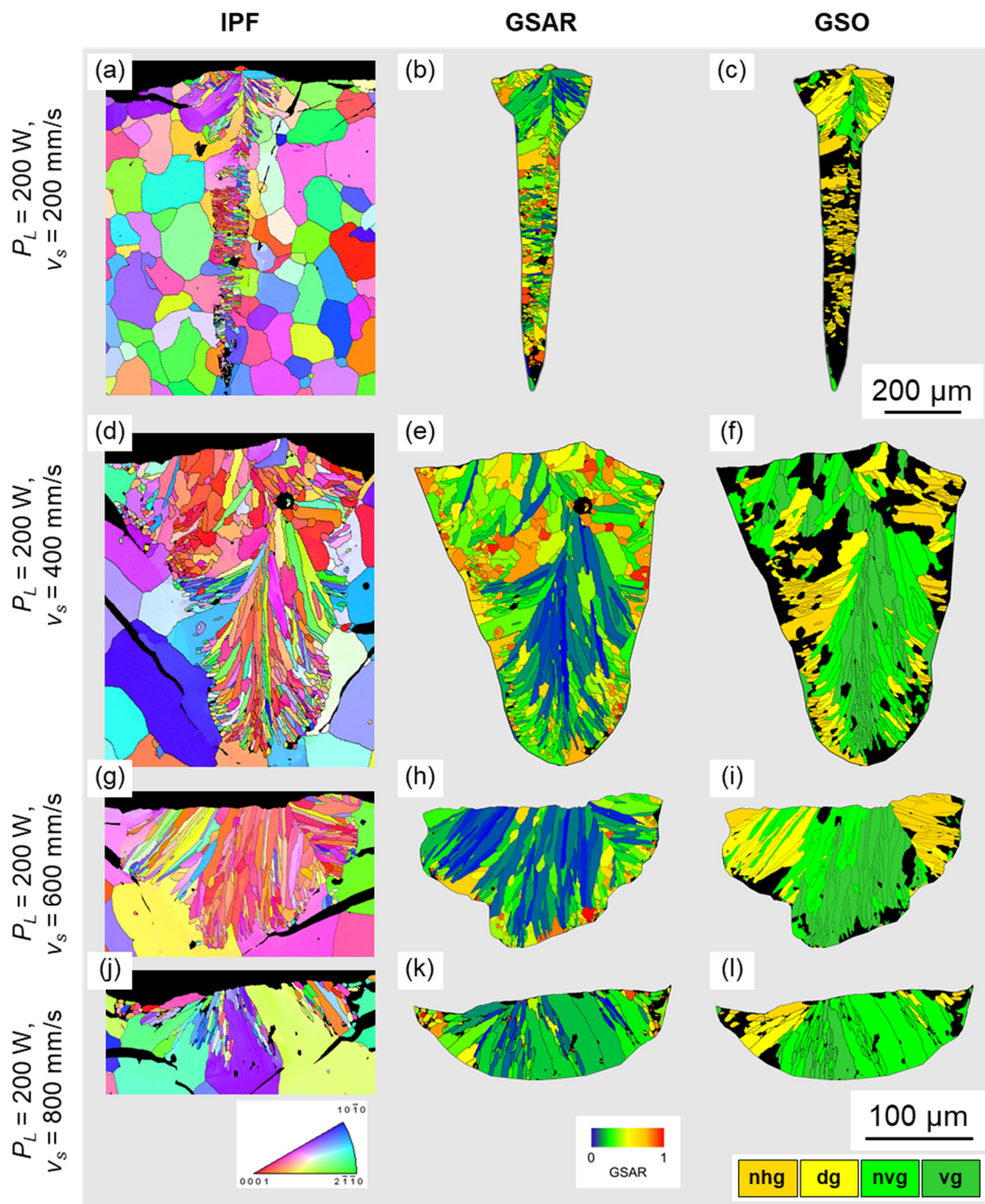


**Figure 4.** EBSD analysis and evaluation of the grain shape anisotropy in samples produced with a constant  $P_L = 200$  W and  $v_s$  of (a–c) 200 mm/s, (d–f) 400 mm/s, (g–i) 600 mm/s and (j–l) 800 mm/s. (a,d,g,j), the inverse pole figure (IPF) maps, show the crystallographic orientation of the grains. (b,e,h,k) show the grain shape aspect ratio (GSAR) map, indicating columnar grown grains with low GSAR ( $>0.5$ ) and equiaxed grains with a higher GSAR ( $>0.5$ ). (c,f,i,l) show the grain shape orientation (GSO) maps, which indicates the direction the grains grew in. Growth direction in the GSO maps is shown in four categories (near-horizontal growth (nhg), diagonal growth (dg), near-vertical growth (nvg), and vertical growth (vg)). A different scale bar is used for (a–c) to account for the much deeper melt-pool.

A scanning speed of 400 mm/s (Figure 4d–f) produces a melt-pool with a depth of  $\sim 280$   $\mu\text{m}$  and a width of  $\sim 210$   $\mu\text{m}$ . With an aspect ratio of  $\sim 1.3$ , this is in the transition from keyhole to heat conduction welding behavior. The melt-pool also shows a higher

proportion of grains with equiaxed growth (GSAR > 0.5). The columnar grains show a growth direction that is mostly vertical in the middle of the melt-pool and more diagonal and horizontal on the sides. On the bottom of the melt-pool, an area of grains can be seen that starts to grow perpendicular to the melt-pool interface but is then suppressed in favor of the vertical grains in the middle. This suggests a stronger temperature gradient inside the melt-pool in the vertical direction. A further reason for the suppressed growth could be the crystallographic orientation of the grains. As explained in Section 1, columnar growth is favored when preferred growth direction and temperature gradient direction match. This might be the case here, where the vertical grains grow perpendicular to the [0001] crystal direction. As established from the literature in Section 1, preferred growth perpendicular to the [0001] crystal direction is assumed for this alloy under the conditions in the melt-pool. Increasing the scanning speed to 600 mm/s (Figure 4g–i) decreases the melt-pool aspect ratio to ~0.6 with a melt-pool depth of ~120  $\mu\text{m}$  and a width of ~210  $\mu\text{m}$ . The GSAR map shows only a few grains with a GSAR > 0.5 and mostly columnar grown grains, the grains in the middle of the melt-pool grow mostly vertical. On the sides of the melt-pool, the grains grow more diagonally or horizontally. The growth direction is mostly perpendicular to the melt-pool interface. A scanning speed of 800 mm/s (Figure 4j–l) produces an even shallower melt-pool. With a depth of ~65  $\mu\text{m}$  and a width of ~200  $\mu\text{m}$  the melt-pool aspect ratio is 0.33. The GSAR map shows almost no equiaxed grown grains with a GSAR > 0.5. With the broad morphology, most grains grow horizontal, only at the side of the melt-pool a few grains grow in diagonal direction. Figure 5 shows the GSO of the accumulated area fractions in the corresponding angular segments. Table 2 also lists the area fractions of the grains with a GSAR value < 0.5 and the area fractions of grains with the GSO in the four angle segments.

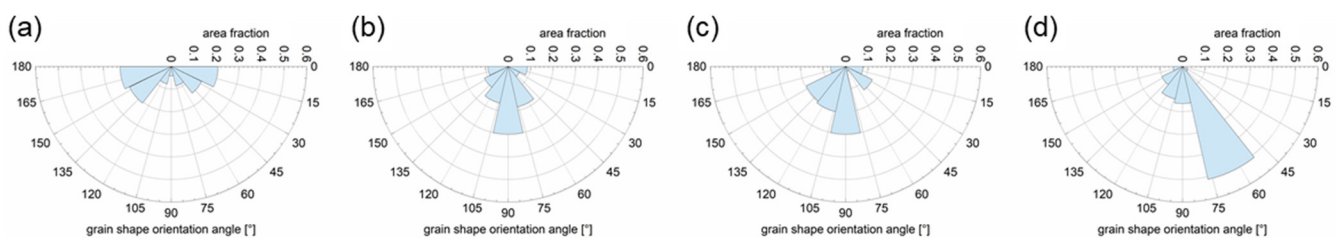


**Figure 5.** Polar plots of the grain shape orientation (GSO) of the samples produced with a constant  $P_L = 200$  W and  $v_s$  of (a) 200 mm/s, (b) 400 mm/s, (c) 600 mm/s and (d) 800 mm/s. The graphs show the area fractions of the grains in the angular segments, described in Section 2—Materials and Methods.

**Table 2.** Area fraction of grains with GSAR < 0.5. Accumulated area fractions of grains with a GSO angle in the four defined angular segments for the samples of the first series—influence of the scan speed. Segment 1, near-horizontal growth (0–25.7° and 154.3–180°). Segment 2, diagonal growth (25.7–51.4° and 128.6–154.3°). Segment 3, near-vertical growth (51.4–77.0° and 102.9–128.6°). Segment 4: vertical growth (77.0–102.9°).

Sample ( $P_L, v_s$ )	GSAR < 0.5 (Columnar) (%)	GSO Area Fraction			
		Segment 1 (%)	Segment 2 (%)	Segment 3 (%)	Segment 4 (%)
200 W, 200 mm/s	66	43.5	35.6	16.7	4.2
200 W, 400 mm/s	75	17.6	17.4	34.9	30.1
200 W, 600 mm/s	89	14.5	32.8	22.7	30.0
200 W, 800 mm/s	93	4.7	12.9	65.9	16.5

As the scan speed increases, the area fraction of columnar grains increases strongly from 66% to 93%. This shows a more pronounced columnar growth in the melt-pool, when using lower line energies by higher scan speeds. Regarding the GSO, in the very deep melt-pool of the sample with 200 mm/s scan speed (Figure 5a), the grains grow mostly horizontally (Segment 1: 43.5%) and diagonally (Segment 2: 35.6%), with only 4.2% of the grain area growing vertically (Segment 4). Using higher scan speeds of 400 mm/s (Figure 5b) and 600 mm/s (Figure 5c), the area fraction of grains with more vertical growth direction increases significantly. With the highest scanning speed of 800 mm/s (Figure 5d), the area fraction with horizontal growth is reduced to only 4.7%.

### 3.2. Influence of the Laser Power

The influence of the laser power on the melt-pool morphology and solidification behavior was examined by varying  $P_L$  (50 W, 100 W, 150 W, 200 W) and leaving  $v_s$  constant at 600 mm/s. The EBSD analysis of the four samples with their inverse pole figure (IPF), grain shape aspect ratio (GSAR) map, and grain shape orientation (GSO) map are given in Figure 6. Table 3 additionally lists the parameters for the melt-pool morphology (depth, width, and aspect ratio), along the mean GSAR values and the grain size with the  $d_{90}$  values for  $Feret_{max}$  and  $Feret_{min}$ .

**Table 3.** Overview of the laser parameters  $P_L$ ,  $v_s$  and  $E_L$ , melt-pool size (depth and width) and aspect ratio, the grain shape aspect ratio GSAR as well as the grain size parameters  $Feret_{max}$   $d_{90}$  and  $Feret_{min}$   $d_{90}$  for the samples of the second series—influence of the laser power.

Sample ( $P_L$ , $v_s$ )	Line Energy $E_L$ (J/mm)	Melt-Pool Depth ( $\mu\text{m}$ )	Melt-Pool Width ( $\mu\text{m}$ )	Melt-Pool Aspect Ratio	GSAR Mean	$Feret_{max}$ $d_{90}$ ( $\mu\text{m}$ )	$Feret_{min}$ $d_{90}$ ( $\mu\text{m}$ )
50 W, 600 mm/s	0.08	25	170	0.15	0.40	24.5	8.8
100 W, 600 mm/s	0.17	80	124	0.65	0.25	44.8	7.3
150 W, 600 mm/s	0.25	63	231	0.27	0.33	44.4	14.7
200 W, 600 mm/s	0.33	118	207	0.57	0.25	65.8	11.6

The sample produced with  $P_L = 50$  W and  $v_s = 600$  mm/s (Figure 6a–c) shows a very shallow melt-pool with a depth of only 25  $\mu\text{m}$  and a width of  $\sim 170$   $\mu\text{m}$ . This accounts for a melt-pool aspect ratio of 0.15, which is the lowest of all samples produced. This is conclusive for the sample with the lowest line energy used ( $E_L = 0.08$  J/mm). The GSAR map shows a few equiaxed grains (GSAR > 0.5), especially at the top and the bottom of the melt-pool. The grains that grow columnar almost all grow in a near-vertical or vertical angle, as can be seen in the GSO map. The melt-pool produced with 100 W laser power (Figure 6d–f) shows a depth of 80  $\mu\text{m}$ , a width of 124  $\mu\text{m}$ , and an aspect ratio of 0.65. This is significantly deeper and narrower than the melt-pools produced with a laser power of 50 W and even 150 W, and thus it appears to be an outlier. The cause of this behavior could not yet be determined but could be reproduced on multiple lines with this parameter. The GSAR map shows predominant columnar growth with only a few grains with a GSAR value > 0.5. The preferred growth direction is again mostly perpendicular to the melt-pool interface, as can be seen in the GSO map. In the middle of the melt-pool, vertical growth dominates, whereas diagonal growth is more dominant on the sides.

Increasing the laser power to 150 W (Figure 6g–i) produces a much wider melt-pool ( $\sim 230$   $\mu\text{m}$ ) with a depth of  $\sim 60$   $\mu\text{m}$ . The melt-pool aspect ratio is 0.27. The GSAR map shows mostly columnar grains in the middle of the melt-pool and some grains with higher GSAR values at the sides. The GSO map shows good vertical growth over the largest part of the melt-pool. Only at the very edges of the melt-pool, the grains grow more

diagonally/horizontally. Using a laser power of 200 W and a scanning speed of 600 mm/s (Figure 6j–l) produces the deepest melt-pool in the series. The sample presented is the same as in Section 3.1 and Figure 3 (see also there for additional details). Increasing the line energy  $E_L$  from 0.08 J/mm to 0.33 J/mm by increasing the laser power  $P_L$  from 50 W to 200 W mainly causes the grain size  $Feret_{max}$  d90 to increase from 24.8  $\mu\text{m}$  to 65.8  $\mu\text{m}$  and the  $Feret_{min}$  d90 to increase from 8.8  $\mu\text{m}$  to 11.6  $\mu\text{m}$ . With the exception of the melt-pool at 100 W, 400 mm/s, the melt-pool aspect ratio increases with increasing  $E_L$  from 0.15 to 0.57, and the mean GSAR decreases from 0.40 to 0.25. This indicated a more columnar growth in the bigger melt-pools produced by higher energy input.

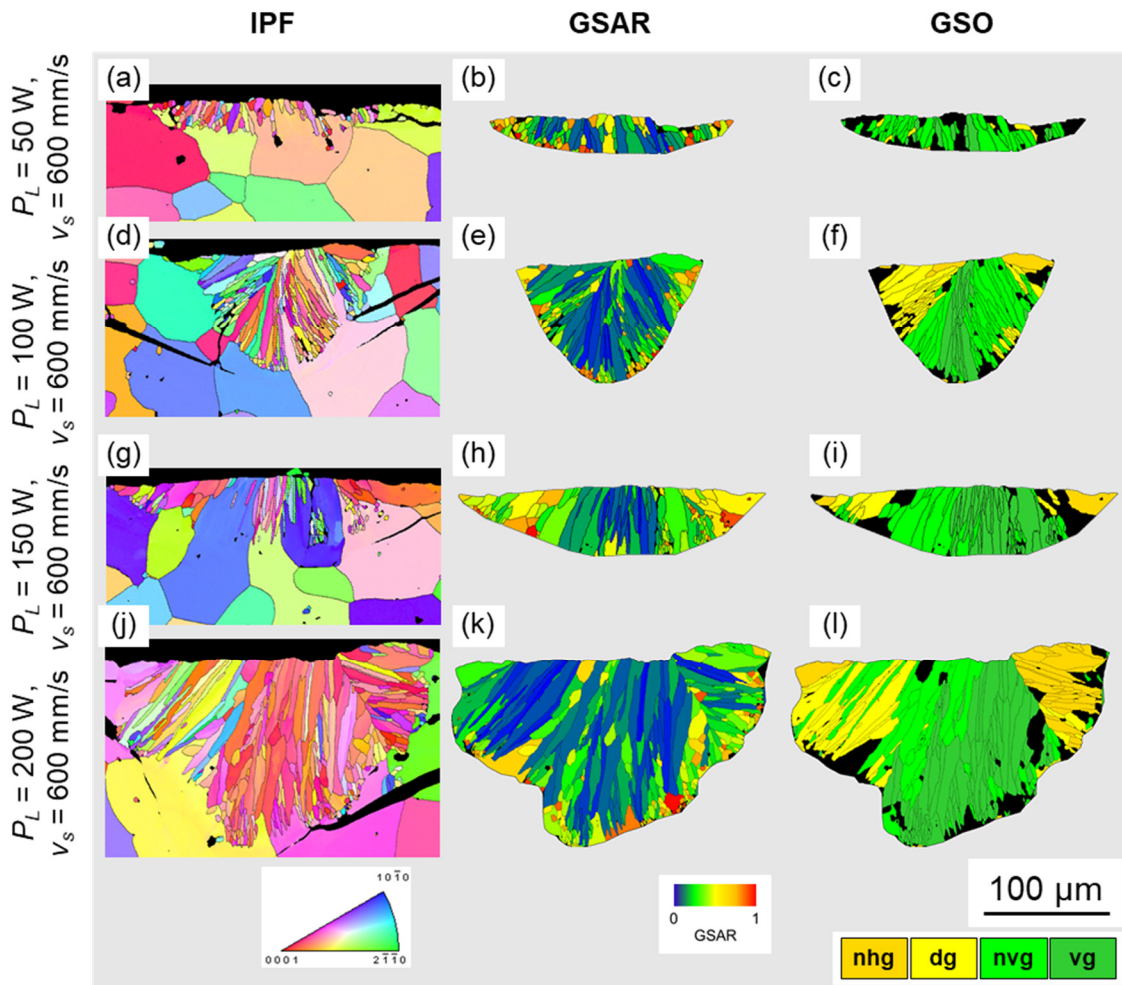


**Figure 6.** EBSD analysis and evaluation of the grain shape anisotropy in samples produced with a constant  $v_s = 600$  mm/s and  $P_L$  of (a–c) 50 W, (d–f) 100 W, (g–i) 150 W and (j–l) 200 W. (a,d,g,j), the inverse pole figure (IPF) maps, show the crystallographic orientation of the grains. (b,e,h,k) show the grain shape aspect ratio (GSAR) map, indicating columnar grown grains with low GSAR (>0.5) and equiaxed grains with a higher GSAR (>0.5). (c,f,i,l) show the grain shape orientation (GSO) maps, which indicates the direction the grains grew in. Growth direction in the GSO maps is shown in four categories (near-horizontal growth (nhg), diagonal growth (dg), near-vertical growth (nvg), and vertical growth (vg)).

Figure 7 shows the GSO of accumulated area fractions in the corresponding angular segments. Table 4 also lists the area fractions of grains with a GSAR value < 0.5 and the area fractions of grains with a GSO in the four angle segments. Looking at the proportions of grain area with a GSAR value < 0.5, the results of the mean GSAR value are also reflected here. Except for the sample at 100 W laser power with a higher-than-expected area of grains

with  $GSAR < 0.5$  (90.0%), the area of grains with a  $GSAR < 0.5$  increases with higher laser power from 70% at 50 W to 89% at 200 W.

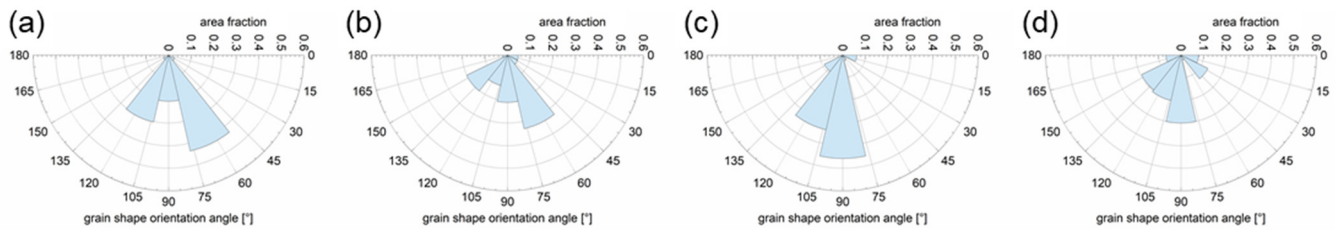


**Figure 7.** Polar plots of the grain shape orientation (GSO) of the samples produced with a constant  $v_s = 600$  mm/s and  $P_L$  of (a) 50 W, (b) 100 W, (c) 150 W, and (d) 200 W. The graphs show the area fractions of the grains in the angular segments described in Section 2—Materials and Methods.

**Table 4.** Area fraction of grains with  $GSAR < 0.5$ . Accumulated area fractions of grains with a GSO angle in the four defined angular segments for the samples of the second series—influence of the laser power. Segment 1, near-horizontal growth ( $0\text{--}25.7^\circ$  and  $154.3\text{--}180^\circ$ ). Segment 2, diagonal growth ( $25.7\text{--}51.4^\circ$  and  $128.6\text{--}154.3^\circ$ ). Segment 3, near-vertical growth ( $51.4\text{--}77.0^\circ$  and  $102.9\text{--}128.6^\circ$ ). Segment 4: vertical growth ( $77.0\text{--}102.9^\circ$ ).

Sample ( $P_L, v_s$ )	GSAR < 0.5 (Columnar) (%)	GSO Area Fraction			
		Segment 1 (%)	Segment 2 (%)	Segment 3 (%)	Segment 4 (%)
50 W, 600 mm/s	70	0.4	5.5	73.7	20.4
100 W, 600 mm/s	90	7.0	25.2	46.9	20.9
150 W, 600 mm/s	85	7.4	10.7	36.2	45.7
200 W, 600 mm/s	89	14.5	32.8	22.7	30.0

All melt-pools in this series produced with a scan speed of 600 mm/s show mostly vertical grain growth. The area fraction of horizontally grown grains (Segment 1) ranges from 0.4% to 14.5%, continually increasing with increasing laser power. Additionally, the area fraction of diagonally grown grains (Segment 2) increases with increasing laser power from 5.5% to 32.8%. In the vertical growth regime, the sample produced with  $P_L = 150$  W shows a maximum of 45.7% of vertical growth in segment 4. However, when considering both segments for nearly vertical growth (Segment 3) and vertical growth (Segment 4) combined, the sample with  $P_L = 50$  W shows a maximum area of 94.1%.

### 3.3. Influence of Laser Power and Scanning Speed at Constant Line Energy

Section three examines the interaction of laser power  $P_L$  and scan speed  $v_s$  by varying both at the same, keeping the line energy  $E_L$  constant at 0.25 J/mm. The samples of this series were produced by using  $P_L = 50$  W and  $v_s = 200$  mm/s,  $P_L = 100$  W and  $v_s = 400$  mm/s,  $P_L = 150$  W and  $v_s = 600$  mm/s,  $P_L = 200$  W and  $v_s = 800$  mm/s. The latter two of these samples were already presented in section one (200 W, 800 mm/s) and section two (150 W, 600 mm/s) of the results chapter. For more detailed information about these samples, the reader is referred to Section 3.1 and Section 3.2, respectively.

The EBSD analysis of the four samples with their inverse pole figure (IPF), grain shape aspect ratio (GSAR) map, and grain shape orientation (GSO) map are given in Figure 8. Table 5 additionally lists the parameters for the melt-pool morphology (depth, width and aspect ratio), along the mean GSAR values and the grain size with the  $d_{90}$  values for  $Feret_{max}$  and  $Feret_{min}$ . With equal line energies used to produce the melt-pools, the depth

of the melt-pools is quite similar, ranging from 52  $\mu\text{m}$  to 65  $\mu\text{m}$ . The melt-pool widths show a bigger spread, ranging from 150  $\mu\text{m}$  to 231  $\mu\text{m}$ . A tendency for deeper and wider melt-pools can be seen when using higher laser power and higher scan speed. The melt-pool aspect ratio ranges from 0.27 to 0.41, with no clear correlation to the laser parameters used. The mean GSAR value for the four samples is also very similar, ranging from 0.28 to 0.33, also showing no clear correlation to the laser parameters. The grain sizes show a wider distribution, with a  $\text{Feret}_{\text{max}}$  d90 ranging from 44.4  $\mu\text{m}$  to 73.6  $\mu\text{m}$  and a  $\text{Feret}_{\text{min}}$  d90 from 10.3  $\mu\text{m}$  to 18.6  $\mu\text{m}$ . The sample with the highest laser power of 200 W and highest scan speed of 800 mm/s shows the highest values for  $\text{Feret}_{\text{max}}$  d90 (73.6  $\mu\text{m}$ ) and  $\text{Feret}_{\text{min}}$  d90 (18.6  $\mu\text{m}$ ). Other than that, no correlation between grain size and laser parameters is visible. At a laser power of 50 W and a scan speed of 200 mm/s (Figure 8a–c), a shallow melt-pool with a depth of 52  $\mu\text{m}$  and a width of 155  $\mu\text{m}$  forms. The GSAR map shows that with a mean GSAR value of 0.33, only a few grains at the sides of the melt-pool grow equiaxed (GSAR > 0.5). Some of these grains might actually grow in a columnar way, but with the short distance to the top of the melt-pool, they cannot grow far enough with respect to their width to be detected as such. The small crack on the left side of the melt-pool (black line in the IPF map) might cause a similar problem by dividing some columnar grains lengthwise. This would lead to a small deviation in the area fractions but should not influence the overall trends.

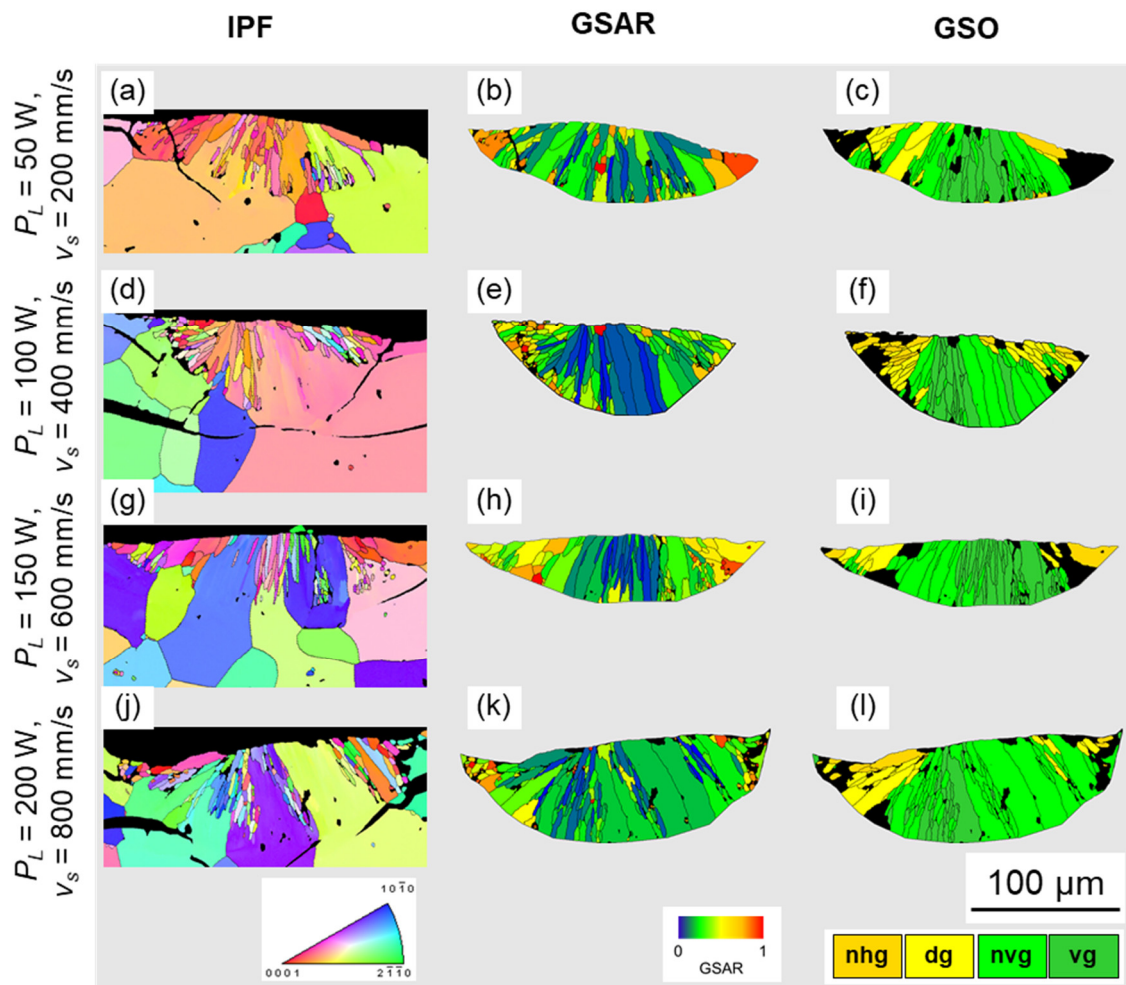
**Table 5.** Overview of the laser parameters  $P_L$ ,  $v_s$  and  $E_L$ , melt-pool size (depth and width), and aspect ratio; the grain shape aspect ratio GSAR and the grain size parameters  $\text{Feret}_{\text{max}}$  d90 and  $\text{Feret}_{\text{min}}$  d90 for the samples of the third series—influence of laser power and scan speed at constant line energy.

Sample ( $P_L$ , $v_s$ )	Line Energy $E_L$ (J/mm)	Melt-Pool Depth ( $\mu\text{m}$ )	Melt-Pool Width ( $\mu\text{m}$ )	Melt-Pool Aspect Ratio (-)	GSAR Mean (-)	$\text{Feret}_{\text{max}}$ d90 ( $\mu\text{m}$ )	$\text{Feret}_{\text{min}}$ d90 ( $\mu\text{m}$ )
50 W, 200 mm/s	0.25	52	155	0.34	0.33	45.1	17.3
100 W, 400 mm/s	0.25	61	150	0.41	0.28	62.6	10.3
150 W, 600 mm/s	0.25	63	231	0.27	0.33	44.4	14.7
200 W, 800 mm/s	0.25	65	200	0.33	0.30	73.6	18.6

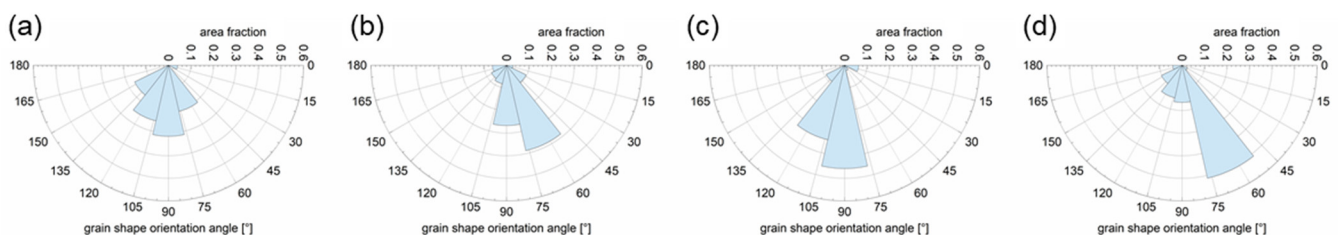
At  $P_L = 100$  W and  $v_s = 400$  W (Figure 8d–f), a higher fraction of smaller grains with higher GSAR values is noticeable at the sides of the melt-pool. These smaller grains are either equiaxed or grow diagonally/horizontally. This corresponds to the melt-pool shape with a depth of ~60  $\mu\text{m}$ , a width of 150  $\mu\text{m}$ , and an aspect ratio of 0.41. This is the highest aspect ratio of the samples in this series produced with an  $E_L = 0.25$  J/mm. This sample shows a phenomenon that is also visible in some of the other samples (e.g., 50 W, 600 mm/s; 100 W, 600 mm/s, both Figure 6). The grains with a GSAR > 0.5 and, therefore, equiaxed growth are mostly smaller grains at the sides of the melt-pool. This corresponds to the literature [26–28], with temperature gradients being the lowest at the sides and the top of the melt-pool, leading to more equiaxed growth. Again, it is visible in the GSO maps (Figure 8c,f,i,l) that the preferred grain growth direction of the columnar grains is more or less perpendicular to the melt-pool interface. Following that, the central region of the melt-pools shows mostly vertical growth, while the sides of the melt-pool are dominated by diagonal and horizontal growth directions.

Figure 9 shows the GSO of accumulated area fractions in the corresponding angular segments. Table 6 additionally lists the area fractions of grains with a GSAR value < 0.5 and the area fractions of grains with a GSO in the four angle segments. All four samples show high area fractions with GSAR < 0.5 of 83.0% (50 W, 200 mm/s) up to 93.0% (200 W, 800 mm/s). The area fractions for the near-vertical and vertical growth (Segments 3 and 4), proportions are similar for all four samples with values of 77.5%, 73.8%, 81.9%, and 82.4%,

respectively. Consequently, the area fractions for horizontal growth are low for all samples, ranging from 4.7% (200 W, 800 mm/s) up to 9.1% (100 W, 400 mm/s).



**Figure 8.** EBSD analysis and evaluation of the grain shape anisotropy in samples produced with a constant  $E_L = 0.25$  J/mm produced by (a–c)  $P_L = 50$  W and  $v_s = 200$  mm/s, (d–f)  $P_L = 100$  W and  $v_s = 400$  mm/s, (g–i)  $P_L = 150$  W and  $v_s = 600$  mm/s and (j–l)  $P_L = 200$  W and  $v_s = 800$  mm/s. (a,d,g,j), the inverse pole figure (IPF) maps, show the crystallographic orientation of the grains. (b,e,h,k) show the grain shape aspect ratio (GSAR) map, indicating columnar grown grains with low GSAR ( $>0.5$ ) and equiaxed grains with a higher GSAR ( $>0.5$ ). (c,f,i,l) show the grain shape orientation (GSO) maps, which indicates the direction the grains grew in. Growth direction in the GSO maps is shown in four categories (near-horizontal growth (nhg), diagonal growth (dg), near-vertical growth (nvg), and vertical growth (vg)).



**Figure 9.** Polar plots of the grain shape orientation (GSO) of the samples produced with a constant  $E_L = 0.25$  J/mm produced by (a)  $P_L = 50$  W and  $v_s = 200$  mm/s, (b)  $P_L = 100$  W and  $v_s = 400$  mm/s, (c)  $P_L = 150$  W and  $v_s = 600$  mm/s and (d)  $P_L = 200$  W and  $v_s = 800$  mm/s. The graphs show the area fractions of the grains in the angular segments, described in Section 2—Materials and Methods.

**Table 6.** Area fraction of grains with GSAR < 0.5. Accumulated area fractions of grains with a GSO angle in the four defined angular segments for the samples of the third series—influence of laser power and scan speed at constant line energy. Segment 1, near-horizontal growth (0–25.7° and 154.3–180°). Segment 2, diagonal growth (25.7–51.4° and 128.6–154.3°). Segment 3, near-vertical growth (51.4–77.0° and 102.9–128.6°). Segment 4: vertical growth (77.0–102.9°).

Sample ( $P_L$ , $v_s$ )	GSAR < 0.5 (Columnar) (%)	GSO Area Fraction			
		Segment 1 (%)	Segment 2 (%)	Segment 3 (%)	Segment 4 (%)
50 W, 200 mm/s	83	5.0	17.5	46.1	31.4
100 W, 400 mm/s	88	9.1	17.1	47.1	26.7
150 W, 600 mm/s	85	7.4	10.7	36.2	45.7
200 W, 800 mm/s	93	4.7	12.9	65.9	16.5

#### 4. Discussion

As proposed from the literature in the Introduction, the main factors that determine the solidification behavior in the melt-pool of structural materials such as steels, Al-, Ti-, or Ni-alloys, are the crystal structure of the material [20], the substrate conditions, and the melt-pool size and shape, which in turn is determined by the used energy density [26–29]. In the case of single laser tracks, this is the line energy  $E_L$ , which is again determined by the laser power  $P_L$  and the scan speed  $v_s$ . According to the literature [28,40–43] a large melt-pool with a low melt-pool aspect ratio (depth/width) is beneficial for columnar dendritic growth. In PBF-LB, this was previously realized by using higher energy densities with higher  $P_L$ . When using a constant energy density, a combination of high  $P_L$  and high  $v_s$  proved beneficial [44–48].

Figure 10a shows the influence of the line energy  $E_L$  on the aspect ratio (depth/width) of the melt-pool produced. As can be seen, the melt-pool aspect ratio increases significantly with the  $E_L$  used. An outlier here is the sample with an  $E_L = 0.17$  J/mm and an aspect ratio of 0.65, which is the sample that was already identified as an outlier (100 W, 600 mm/s) in Section 3.2 (Results). Of the samples examined, only two parameters led to an aspect ratio > 1 (melt-pool is deeper than wide). This is caused by a difference in the two different process regimes, with a transition from heat-conduction welding to keyhole welding at higher energy densities [30,31].

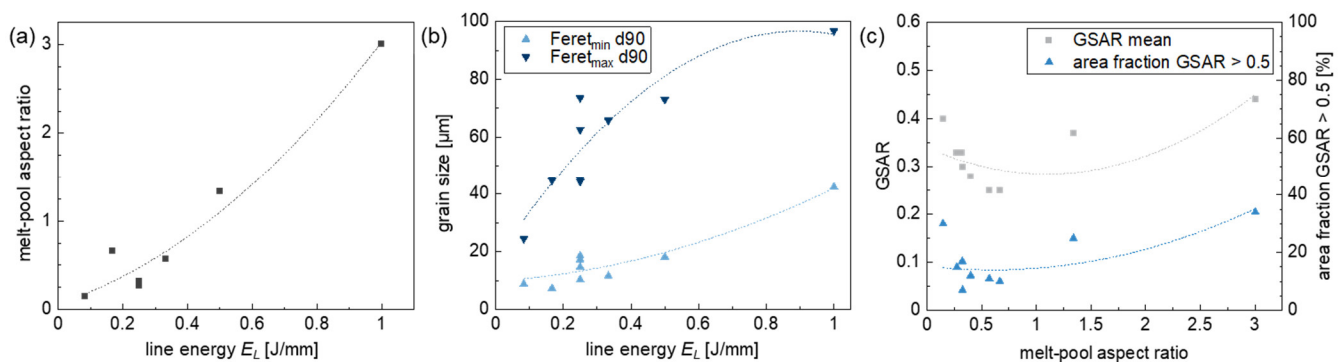


**Figure 10.** (a) Melt-pool aspect ratio increases with increasing line energy  $E_L$ . (b) The grain size (Feret<sub>max</sub> d90 and Feret<sub>min</sub> d90) increases with increasing line energy. (c) GSAR mean value and grain area fraction with GSAR values > 0.5 (equiaxed grains) in dependence of the melt-pool aspect ratio. GSAR mean value and grain area fraction with GSAR > 0.5 seem to have an optimum for a melt-pool aspect ratio around 0.6. Graphs contain trendlines using a polynomial fit.

All samples produced with an  $E_L < 0.5$  are clearly in the regime of heat conduction welding with shallower melt-pools. At an  $E_L = 0.5$  J/mm (200 W, 400 mm/s), a behavior in transition of heat conduction to keyhole welding is observed. This leads to a melt-pool with a depth of  $\sim 280$   $\mu\text{m}$ , a width of  $\sim 210$   $\mu\text{m}$ , and an aspect ratio of 1.34. At  $E_L = 1.00$  J/mm (200 W, 200 mm/s), the process regime is keyhole welding, producing a melt-pool that is significantly deeper ( $\sim 790$   $\mu\text{m}$ ) than it is wide ( $\sim 260$   $\mu\text{m}$ ), with an aspect ratio of 3.

In most metallic materials, the grain size is a crucial factor regarding its properties. While structural materials such as steels often require smaller grain sizes for improved mechanical properties [49]. Because the nanostructure that leads to the permanent magnetic properties of  $(\text{CoCuFeZr})_{17}\text{Sm}_2$  is not fully formed at the grain boundaries [50,51], a larger grain size is beneficial for the magnetic properties [52], especially the coercivity. Looking at the dependence of the grain size, Figure 10b shows the dependence of the grain size parameters  $\text{Feret}_{\text{max}} d_{90}$  and  $\text{Feret}_{\text{min}} d_{90}$  of the line energy  $E_L$ . Values for  $\text{Feret}_{\text{max}}$  and  $\text{Feret}_{\text{min}}$  both rise with increasing line energy. At equal  $E_L$  (0.25 J/mm), produced with different combinations of  $P_L/v_s$ , a quite large spread of grain sizes can be seen in the  $\text{Feret}_{\text{max}}$ . As mentioned before in the results (Section 3.3), there is a tendency for higher grain sizes when using higher  $P_L$  and  $v_s$  for the same  $E_L$ . The grain size in all melt-pools is significantly smaller than the grain size of the substrate ( $\text{Feret}_{\text{min}} d_{90} = 88$   $\mu\text{m}$ ;  $\text{Feret}_{\text{max}} = 152$   $\mu\text{m}$ ). Taking into account the large spread of grain sizes throughout the different parameters and the difference in grain sizes between melt-pools and substrate, the grain size of the substrate seems to have only marginal influence on the resulting microstructure in the melt-pool. Looking at the dependence of the GSAR from the melt-pool aspect ratio in Figure 10c, a trend becomes visible. At the lowest melt-pool aspect ratios (e.g., 50 W, 600 mm/s with an aspect ratio of 0.15), quite high GSAR mean values of up to 0.4 and area fractions with  $\text{GSAR} > 0.5$  of 30% can be found. This is almost as high as the values of 0.44 and 34%, respectively, achieved in the keyhole welding regime with very high melt-pool aspect ratios (200 W, 200 mm/s with an aspect ratio of 3). The GSAR values (mean GSAR as well as the area fraction with  $\text{GSAR} > 0.5$ ) seem to approach an optimum for columnar grain growth (low GSAR values) at a melt-pool aspect ratio of around 0.6. The lowest GSAR mean values and lowest area fractions with  $\text{GSAR} > 0.5$  were achieved at melt-pool aspect ratios of 0.57 (200 W, 600 mm/s) and 0.65 (100 W, 600 mm/s), with GSAR mean values of 0.25 (both) and  $\text{GSAR} > 0.5$  area fractions of 11% and 10%, respectively.

To further assess and compare the shape anisotropy of grains in the melt-pool, the mean angular deviation of the GSO from the vertical axis was calculated for each parameter set. By plotting the mean GSO angle deviation separately for the three series of experiments described in Section 3, the influence of the different process parameters can be evaluated. The mean angle deviation of the GSO in dependence of the scan speed, the laser power, and the combination of both at constant line energy is visualized in Figure 11a–c, respectively.

The influence of the scan speed shows a strong increase of the angle deviation for the lowest scan speed of 200 mm/s. As explained before, this is the only parameter in the experiments that produced a very deep, keyhole type melt-pool. Following that behavior, many of the grains showed equiaxed growth or a more horizontal growth direction. The remaining samples show a mean angle deviation between  $34.2^\circ$  and  $29.2^\circ$ , with a minimum at the highest scan speed of 800 mm/s. This shows a tendency of favored vertical growth orientation at higher scan speeds. At constant scan speed, varying the laser power from 50 W to 200 W causes the mean angle deviation to increase from  $22.5^\circ$  to  $34.2^\circ$ . With the outlier at 100 W, which was described in more detail in Section 3.2, the trend is not completely clear, but lower laser power seems to promote a more vertical growth direction. Looking at the mean angle deviation at constant line energy of 0.25 J/mm, produced by different combinations of  $P_L$  and  $v_s$ , the angle is quite similar for all samples. Ranging from  $23.1^\circ$  to  $29.2^\circ$ , all samples with this line energy show quite good vertical growth. With a minimum at the sample produced with  $P_L = 150$  W and  $v_s = 200$  mm/s, combinations with higher scan speed and higher laser power seem to slightly favor a more vertical growth direction of the columnar grains.

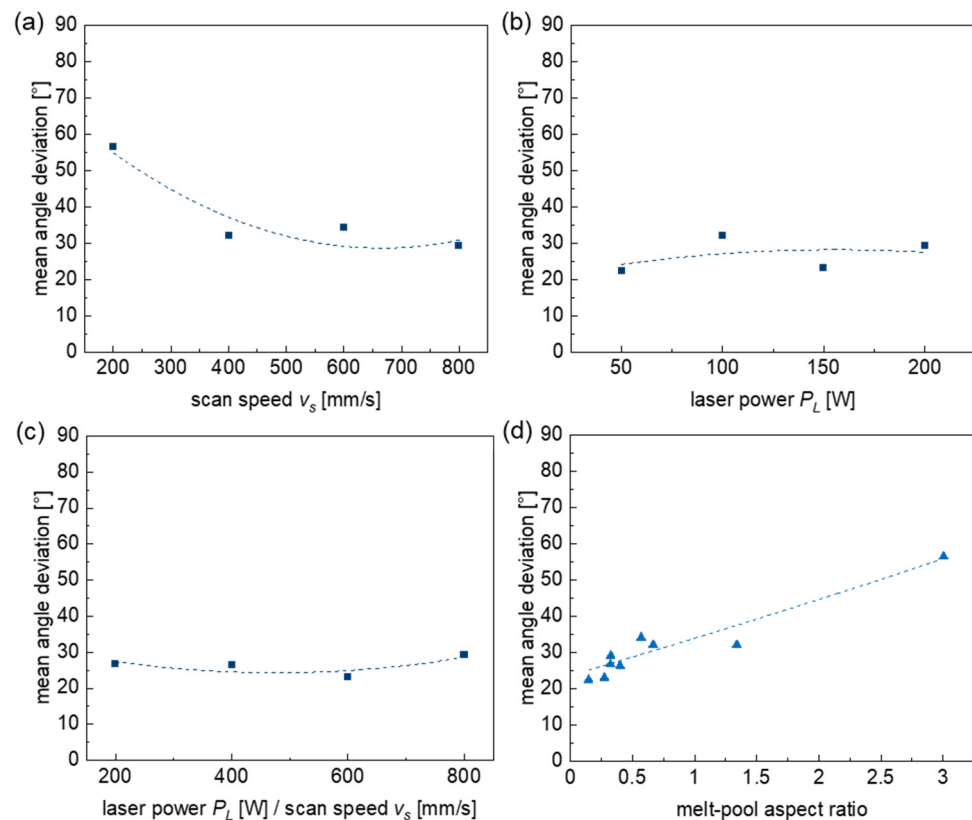


**Figure 11.** Mean angle deviation of the GSO from strictly vertical growth in dependence of (a) the scan speed at constant laser power, (b) the laser power at constant scan speed, (c) the combination of laser power and scan speed at a constant line energy, and (d) the melt-pool aspect ratio. All graphs contain trendlines using a polynomial fit.

The mean angle deviation in dependence of the melt-pool aspect ratio is visualized in Figure 11d. It can be seen that the mean angle deviation increases with increasing melt-pool aspect ratio. At lower melt-pool aspect ratios (around  $< 0.5$ ), the angular deviation increases rapidly. This clearly shows that vertical growth is favored in wider, shallower melt-pools. This behavior is consistent with the literature on the fundamentals of solidification [20] and with the results produced on aluminum alloys [26]. The grains grow along the temperature gradient that lies perpendicular to the melt-pool interface [26]. If we take into account the area fraction of the melt-pool that grows equiaxed without a growth direction (area fraction with  $GSAR > 0.5$ , Figure 11a) and compare this to the mean angle deviation, the optimum for columnar growth with vertical growth direction now seems to be at slightly higher melt-pool aspect ratios of around 0.3–0.5 instead of at the lowest aspect ratio ( $\sim 0.15$ ). While the shallowest melt-pools show the best degree of orientation of the grain shape, with a minimum mean deviation of  $22.5^\circ$ , they also exhibit higher area fractions of equiaxed grains. At slightly higher melt-pool aspect ratios, the angular deviation is still similarly low (e.g.,  $26.4^\circ$  at a melt-pool aspect ratio of 0.4) but with lower area fractions of equiaxed grains. This result is consistent with the previously presented literature on PBF-LB processing of steels and Ti-alloys [28,40–43]. This suggests low melt-pool aspect ratios but also bigger melt-pool areas for columnar growth. In addition to the reported results, the IPF maps of melt-pools and substrate show several occasions, where the crystallographic orientation of the substrate is almost identical to the grains that grow above them in the melt-pool. These grains exhibit strong columnar growth, which is mostly undisturbed up to the surface of the melt-pool. This is probably the result of a good match between the direction of the predominant temperature gradient and the crystal direction of the substrate. Meaning, the preferred growth direction of the crystal lattice is oriented along the temperature gradient in the melt-pool, which provides optimal conditions for columnar dendritic growth [20,53].

The single-track experiments represent a solid basis for future research. However, the processing parameters have to be fine-tuned for the PBF-LB process, e.g., the absorption of the laser in the powder bed, which is usually much higher than on the surface of a bulk sample because of multiple reflections and absorption on the powder particles [54]. To account for that as good as possible on the bulk material, samples were roughly ground before the laser experiments to minimize the reflection of the laser on the surface. A shift of parameters to a lower energy input to achieve similar results is expected in PBF-LB processing. Additionally, in the PBF-LB process, the laser tracks, as well as the stacked layers, naturally overlap each other to form a dense part. To summarize this, the parameters from the single-track experiments might require adjustments but will provide valuable indications on how to tune the laser parameters to improve the texture of solidification microstructures.

## 5. Conclusions

In this work a method is introduced to evaluate the solidification microstructure with growth shape (equiaxed/columnar) and the growth direction of columnar grains from EBSD analysis. Columnar dendritic growth and a uniform growth direction are seen as prerequisites for the PBF-LB additive manufacturing of permanent magnets with a textured microstructure and anisotropic magnetic properties in the future. The method is used to study the influence of scanning speed, laser power and line energy on the solidification microstructure in the laser melt-pool of single-track experiments on  $(\text{CoCuFeZr})_{17}\text{Sm}_2$  sintered magnets.

Starting from conventional EBSD analysis, the grain shape aspect ratio (GSAR) is analyzed to distinguish between equiaxed grains (GSAR values  $> 0.5$ ) and columnar grains (GSAR values  $< 0.5$ ). For columnar grains, the grain shape orientation (GSO) is determined using an ellipsoid fit in the grains. The grain shape orientation angle (relative to the sample surface) is used to determine the preferred growth directions of grains in the melt-pool. The average deviation of the GSO from the vertical direction is introduced as a parameter for the evaluation and comparison of the growth direction of the whole melt-pool.

Shallow melt-pools were found to favor columnar dendritic growth. The area fraction of columnar grains reaches a maximum of  $\sim 90\%$  at melt-pool aspect ratios around 0.3–0.5. It was found that higher scanning speeds seem favorable for columnar growth with vertical growth direction by the creation of a shallow melt-pool with a low aspect ratio. Higher laser power was found to favor columnar growth with vertical growth direction only at lower line energies. At high line energy, high laser power led to melt-pools with high aspect ratios which was detrimental to the oriented columnar growth. The highest influence was found in the line energy resulting from the combination of laser power and scan speed. Lower line energies led to melt-pools with low aspect ratios that promote columnar growth with a vertical growth direction. At a constant line energy, the combination of high laser power and high scanning speed showed tendencies towards higher area fractions of columnar grains and slightly higher area fractions of grains with vertical growth direction. Additionally, it led to larger grain sizes, which are beneficial for the magnetic properties of  $(\text{CoCuFeZr})_{17}\text{Sm}_2$ .

Because the columnar grains in the melt-pool always grow along the temperature gradient, the presented method for analysis of the growth direction can also be used to reconstruct and visualize the temperature gradients that were present in the melt-pool during solidification through the GSO. This will be used in a forthcoming publication, which addresses the crystallographic orientations in directional solidification of  $(\text{CoCuFeZr})_{17}\text{Sm}_2$  in the laser melt-pool.

**Author Contributions:** Conceptualization, F.T., R.L., G.S. and D.G.; methodology, F.T., R.L., G.S. and D.G.; software, F.T.; validation, F.T., R.L., G.S. and D.G.; formal analysis, F.T.; investigation, F.T., R.L., G.S. and D.G.; resources, G.S. and D.G.; data curation, F.T., R.L., G.S. and D.G.; writing—original draft preparation, F.T., R.L., G.S. and D.G.; writing—review and editing, F.T., R.L., G.S. and D.G.; visualization, F.T.; supervision, G.S. and D.G.; project administration, D.G.; funding acquisition, D.G. All authors have read and agreed to the published version of the manuscript.

**Funding:** This research was funded by the Deutsche Forschungsgemeinschaft (DFG, German Research Foundation) within the scope of the project Comet, project number 516736439. Publication funded by Aalen University of Applied Sciences.

**Data Availability Statement:** The original contributions presented in the study are included in the article; further inquiries can be directed to the corresponding authors.

**Acknowledgments:** The authors thank Dominic Hohs, Gerhard Martinek, Julian Schurr, Tim Schubert, and Emanuel Wengenmayr for assistance during preparation, processing, and analysis of the samples and for fruitful discussions (all Aalen University). The authors thank Urs Wyss from Arnold Magnetic Technologies for providing Co–Sm isotropic sintered magnets for the experiments performed.

**Conflicts of Interest:** The authors declare no conflicts of interest.

## References

1. Herbst, J.F. R2Fe14 B materials: Intrinsic properties and technological aspects. *Rev. Mod. Phys.* **1991**, *63*, 819–898. [CrossRef]
2. Kim, A.S.; Camp, F.E.; Stadelmaier, H.H. Relation of remanence and coercivity of Nd,(Dy)-Fe,(Co)-B sintered permanent magnets to crystallite orientation. *J. Appl. Phys.* **1994**, *76*, 6265–6267. [CrossRef]
3. Goll, D.; Vogelgsang, D.; Pflanz, U.; Hohs, D.; Grubesa, T.; Schurr, J.; Bernthaler, T.; Kolb, D.; Riegel, H.; Schneider, G. Refining the Microstructure of Fe-Nd-B by Selective Laser Melting. *Phys. Status Solidi RRL* **2019**, *13*, 1800536. [CrossRef]
4. Goll, D.; Trauter, F.; Braun, P.; Laukart, J.; Loeffler, R.; Golla-Schindler, U.; Schneider, G. Additive Manufacturing of Permanent Magnets Based on (CoCuFeZr)<sub>17</sub>Sm<sub>2</sub>. *Phys. Status Solidi RRL* **2021**, *15*, 2100294. [CrossRef]
5. Goll, D.; Trauter, F.; Loeffler, R.; Gross, T.; Schneider, G. Additive Manufacturing of Textured FePrCuB Permanent Magnets. *Micromachines* **2021**, *12*, 1056. [CrossRef]
6. Goll, D.; Schurr, J.; Trauter, F.; Schanz, J.; Bernthaler, T.; Riegel, H.; Schneider, G. Additive manufacturing of soft and hard magnetic materials. *Procedia CIRP* **2020**, *94*, 248–253. [CrossRef]
7. Périgo, E.A.; Jacimovic, J.; García Ferré, F.; Scherf, L.M. Additive manufacturing of magnetic materials. *Addit. Manuf.* **2019**, *30*, 100870. [CrossRef]
8. Bittner, F.; Thielsch, J.; Drossel, W.-G. Microstructure and magnetic properties of Nd-Fe-B permanent magnets produced by laser powder bed fusion. *Scr. Mater.* **2021**, *201*, 113921. [CrossRef]
9. Bittner, F.; Thielsch, J.; Drossel, W.-G. Unexpected Coercivity Enhancement >1T for Nd-Fe-B Permanent Magnets With 20 wt% Nd Produced by Laser Powder Bed Fusion. *IEEE Trans. Magn.* **2022**, *58*, 1–5. [CrossRef]
10. Magnequench. Magnequench MQP Powder: MQP-S-11-9-20001-070 Isotropic Powder. Available online: <https://mqjtechnology.com/product/mqp-s-11-9-20001/> (accessed on 5 September 2024).
11. Goll, D.; Trauter, F.; Bernthaler, T.; Schanz, J.; Riegel, H.; Schneider, G. Additive Manufacturing of Bulk Nanocrystalline FeNdB Based Permanent Magnets. *Micromachines* **2021**, *12*, 538. [CrossRef]
12. Tosoni, O.; Borges Mendonça, E.; Reijonen, J.; Antikainen, A.; Schäfer, L.; Riegg, S.; Gutfleisch, O. High-coercivity copper-rich Nd-Fe-B magnets by powder bed fusion using laser beam method. *Addit. Manuf.* **2023**, *64*, 103426. [CrossRef]
13. Kwon, H.W.; Bowen, P.; Harris, I.R. A study of Pr-Fe-B-Cu permanent magnetic alloys. *J. Alloys Compd.* **1992**, *182*, 233–242. [CrossRef]
14. Mycock, G.J.; Faria, R.; Harris, I.R. The microstructures and magnetic properties of some cast and annealed Pr-Fe-Cu-B alloys. *J. Alloys Compd.* **1993**, *201*, 23–28. [CrossRef]
15. Shimoda, T.; Akioka, K.; Kobayashi, O.; Yamagami, T.; Ohki, T.; Miyagawa, M.; Yuri, T. Hot-working behavior of cast Pr-Fe-B magnets. *IEEE Trans. Magn.* **1989**, *25*, 4099–4104. [CrossRef]
16. Schäfer, L.; Skokov, K.; Liu, J.; Maccari, F.; Braun, T.; Riegg, S.; Radulov, I.; Gassmann, J.; Merschroth, H.; Harbig, J.; et al. Design and Qualification of Pr–Fe–Cu–B Alloys for the Additive Manufacturing of Permanent Magnets. *Adv. Funct. Mater.* **2021**, *11*, 2102148. [CrossRef]
17. Arnold Magnetic Technologies Corporation. Recoma® Sintered Samarium Cobalt Magnets. Available online: <https://www.arnoldmagnetics.de/products/recoma-samarium-cobalt-magnets/> (accessed on 5 September 2024).
18. Schleifenbaum, H.; Meiners, W.; Wissenbach, K.; Hinke, C. Individualized production by means of high power Selective Laser Melting. *CIRP J. Manuf. Sci. Technol.* **2010**, *2*, 161–169. [CrossRef]
19. Gu, D.D.; Meiners, W.; Wissenbach, K.; Poprawe, R. Laser additive manufacturing of metallic components: Materials, processes and mechanisms. *Int. Mater. Rev.* **2012**, *57*, 133–164. [CrossRef]
20. Kurz, W.; Fisher, D.J. *Fundamentals of Solidification*, 3rd ed.; Trans Tech Publication: Aedermannsdorf, Switzerland, 1992; ISBN 0878495223.
21. Zhang, T.; Liu, H.; Ma, Z.; Jiang, C. Single crystal growth and magnetic properties of 2:17-type SmCo magnets. *J. Alloys Compd.* **2015**, *637*, 253–256. [CrossRef]
22. Plugaru, N.; Rubín, J.; Bartolomé, J. Structural and magnetic investigation of Co-rich Sm–Co unidirectionally solidified alloys. *J. Alloys Compd.* **2007**, *433*, 129–139. [CrossRef]

23. Kurz, W.; Trivedi, R. Microstructure and Phase Selection in Laser Treatment of Materials. *J. Eng. Mater. Technol.* **1992**, *114*, 450–458. [[CrossRef](#)]
24. Wang, Y.; Shi, J.; Liu, Y. Competitive grain growth and dendrite morphology evolution in selective laser melting of Inconel 718 superalloy. *J. Cryst. Growth* **2019**, *521*, 15–29. [[CrossRef](#)]
25. Kou, S. *Welding Metallurgy*, 2nd ed.; Wiley-Interscience: Hoboken, NJ, USA, 2003; ISBN 0471434914.
26. Thijs, L.; Kempen, K.; Kruth, J.-P.; van Humbeeck, J. Fine-structured aluminium products with controllable texture by selective laser melting of pre-alloyed AlSi10Mg powder. *Acta Mater.* **2013**, *61*, 1809–1819. [[CrossRef](#)]
27. Krakhmalev, P.; Fredriksson, G.; Svensson, K.; Yadroitsev, I.; Yadroitsava, I.; Thuvander, M.; Peng, R. Microstructure, Solidification Texture, and Thermal Stability of 316 L Stainless Steel Manufactured by Laser Powder Bed Fusion. *Metals* **2018**, *8*, 643. [[CrossRef](#)]
28. Köhnen, P.; Létang, M.; Voshage, M.; Schleifenbaum, J.H.; Haase, C. Understanding the process-microstructure correlations for tailoring the mechanical properties of L-PBF produced austenitic advanced high strength steel. *Addit. Manuf.* **2019**, *30*, 100914. [[CrossRef](#)]
29. Zhang, S.; Lei, Y.; Chen, Z.; Wei, P.; Liu, W.; Yao, S.; Lu, B. Effect of Laser Energy Density on the Microstructure and Texture Evolution of Hastelloy-X Alloy Fabricated by Laser Powder Bed Fusion. *Materials* **2021**, *14*, 4305. [[CrossRef](#)]
30. Bass, M. (Ed.) *Laser Materials Processing*; North-Holland: Amsterdam, The Netherlands, 1983; ISBN 0444863966.
31. Ready, J.F. *Industry Government Education, MPI. LIA Handbook of Laser Materials Processing*, 1st ed.; Laser Institute of America; Magnolia Publication: Orlando, FL, USA, 2001; ISBN 978-3-540-41770-5.
32. Nath, A.K.; Sridhar, R.; Ganesh, P.; Kaul, R. Laser power coupling efficiency in conduction and keyhole welding of austenitic stainless steel. *Sadhana* **2002**, *27*, 383–392. [[CrossRef](#)]
33. Ion, J.C. Laser beam welding of wrought aluminium alloys. *Sci. Technol. Weld. Join.* **2000**, *5*, 265–276. [[CrossRef](#)]
34. Antikainen, A.; Reijonen, J.; Lagerbom, J.; Lindroos, M.; Pinomaa, T.; Lindroos, T. Single-Track Laser Scanning as a Method for Evaluating Printability: The Effect of Substrate Heat Treatment on Melt Pool Geometry and Cracking in Medium Carbon Tool Steel. *J. Mater. Eng Perform* **2022**, *31*, 8418–8432. [[CrossRef](#)]
35. Aboulkhair, N.T.; Maskery, I.; Tuck, C.; Ashcroft, I.; Everitt, N.M. On the formation of AlSi10Mg single tracks and layers in selective laser melting: Microstructure and nano-mechanical properties. *J. Mater. Process. Technol.* **2016**, *230*, 88–98. [[CrossRef](#)]
36. Yadroitsev, I.; Gusarov, A.; Yadroitsava, I.; Smurov, I. Single track formation in selective laser melting of metal powders. *J. Mater. Process. Technol.* **2010**, *210*, 1624–1631. [[CrossRef](#)]
37. Aversa, A.; Moshiri, M.; Librera, E.; Hadi, M.; Marchese, G.; Manfredi, D.; Lorusso, M.; Calignano, F.; Biamino, S.; Lombardi, M.; et al. Single scan track analyses on aluminium based powders. *J. Mater. Process. Technol.* **2018**, *255*, 17–25. [[CrossRef](#)]
38. Fan, Z.; Lu, M.; Huang, H. Selective laser melting of alumina: A single track study. *Ceram. Int.* **2018**, *44*, 9484–9493. [[CrossRef](#)]
39. Ghosh, S.; Ma, L.; Levine, L.E.; Ricker, R.E.; Stoudt, M.R.; Heigel, J.C.; Guyer, J.E. Single-Track Melt-Pool Measurements and Microstructures in Inconel 625. *JOM* **2018**, *70*, 1011–1016. [[CrossRef](#)]
40. Kreitchberg, A.; Brailovski, V.; Sheremetyev, V.; Prokoshkin, S. Effect of Laser Powder Bed Fusion Parameters on the Microstructure and Texture Development in Superelastic Ti–18Zr–14Nb Alloy. *Shap. Mem. Superelasticity* **2017**, *3*, 361–372. [[CrossRef](#)]
41. Andreau, O.; Koutiri, I.; Peyre, P.; Penot, J.-D.; Saintier, N.; Pessard, E.; de Terris, T.; Dupuy, C.; Baudin, T. Texture control of 316L parts by modulation of the melt pool morphology in selective laser melting. *J. Mater. Process. Technol.* **2019**, *264*, 21–31. [[CrossRef](#)]
42. Cepeda-Jiménez, C.M.; Potenza, F.; Magalini, E.; Luchin, V.; Molinari, A.; Pérez-Prado, M.T. Effect of energy density on the microstructure and texture evolution of Ti-6Al-4V manufactured by laser powder bed fusion. *Mater. Charact.* **2020**, *163*, 110238. [[CrossRef](#)]
43. de Moura Nobre, R.; de Moraes, W.A.; Vasques, M.T.; Guzmán, J.; Rodrigues Junior, D.L.; Oliveira, H.R.; Falcão, R.B.; Landgraf, F.J.G. Role of laser powder bed fusion process parameters in crystallographic texture of additive manufactured Nb–48Ti alloy. *J. Mater. Res. Technol.* **2021**, *14*, 484–495. [[CrossRef](#)]
44. Niendorf, T.; Leuders, S.; Riemer, A.; Richard, H.A.; Tröster, T.; Schwarze, D. Highly Anisotropic Steel Processed by Selective Laser Melting. *Met. Mater. Trans B* **2013**, *44*, 794–796. [[CrossRef](#)]
45. Niendorf, T.; Leuders, S.; Riemer, A.; Brenne, F.; Tröster, T.; Richard, H.A.; Schwarze, D. Functionally Graded Alloys Obtained by Additive Manufacturing. *Adv. Eng. Mater.* **2014**, *16*, 857–861. [[CrossRef](#)]
46. Niendorf, T.; Brenne, F.; Schaper, M.; Riemer, A.; Leuders, S.; Reimche, W.; Schwarze, D.; Maier, H.J. Labelling additively manufactured parts by microstructural gradation—Advanced copy-proof design. *RPJ* **2016**, *22*, 630–635. [[CrossRef](#)]
47. Brenne, F.; Leuders, S.; Niendorf, T. On the Impact of Additive Manufacturing on Microstructural and Mechanical Properties of Stainless Steel and Ni-base Alloys. *Bergund Hüttenmännische Monatshefte* **2017**, *162*, 199–202. [[CrossRef](#)]
48. Ehsan Saghayan, S.; Nematollahi, M.; Toker, G.; Hinojos, A.; Shayesteh Moghaddam, N.; Saedi, S.; Lu, C.Y.; Javad Mahtabi, M.; Mills, M.J.; Elahinia, M.; et al. Effect of hatch spacing and laser power on microstructure, texture, and thermomechanical properties of laser powder bed fusion (L-PBF) additively manufactured NiTi. *Opt. Laser Technol.* **2022**, *149*, 107680. [[CrossRef](#)]
49. Lasalmonie, A.; Strudel, J.L. Influence of grain size on the mechanical behaviour of some high strength materials. *J. Mater. Sci.* **1986**, *21*, 1837–1852. [[CrossRef](#)]
50. Zhou, X.; Song, X.; Jia, W.; Xiao, A.; Yuan, T.; Ma, T. Identifications of SmCo<sub>5</sub> and Sm+1Co<sub>5</sub>–1-type phases in 2:17-type Sm-Co-Fe-Cu-Zr permanent magnets. *Scr. Mater.* **2020**, *182*, 1–5. [[CrossRef](#)]

51. Braun, P.; Laukart, J.; Golla-Schindler, U.; Löffler, R.; Goll, D.; Schneider, G. Analysis of microstructure evolution during heat treatment of CoSm permanent magnets using high-resolution scanning electron microscopy. *Pract. Metallogr.* **2022**, *59*, 188–198. [[CrossRef](#)]
52. Palit, M.; Rajkumar, D.M.; Pandian, S.; Kamat, S.V. Effect of grain size on microstructure and magnetic properties of  $\text{Sm}_2(\text{Co,Cu,Fe,Zr})_{17}$  permanent magnets. *Mater. Chem. Phys.* **2016**, *179*, 214–222. [[CrossRef](#)]
53. Ishimoto, T.; Hagihara, K.; Hisamoto, K.; Sun, S.-H.; Nakano, T. Crystallographic texture control of beta-type Ti–15Mo–5Zr–3Al alloy by selective laser melting for the development of novel implants with a biocompatible low Young's modulus. *Scr. Mater.* **2017**, *132*, 34–38. [[CrossRef](#)]
54. Gusarov, A.V.; Kruth, J.-P. Modelling of radiation transfer in metallic powders at laser treatment. *Int. J. Heat Mass Transf.* **2005**, *48*, 3423–3434. [[CrossRef](#)]

**Disclaimer/Publisher's Note:** The statements, opinions and data contained in all publications are solely those of the individual author(s) and contributor(s) and not of MDPI and/or the editor(s). MDPI and/or the editor(s) disclaim responsibility for any injury to people or property resulting from any ideas, methods, instructions or products referred to in the content.